Direct laser writing of vapour-responsive photonic arrays

Colm Delaney,‡[a] Jing Qian, ‡[b] Xia Zhang [b], Radislav Potyrailo[c], A. Louise Bradley[b]* and Larisa Florea[a]*

Using direct laser writing, arrays of optically responsive ionogel structures were fabricated. To demonstrate their responsive nature, visible colour changes in the presence different solvent vapours were investigated. This represents a new departure for photonic structural colouration, in which the fabricating structure shows a programmable, controllable, and dynamic stimuli response.

Introduction

Photonic sensors offer an adaptable means of detecting analytes in the gaseous state, with minimal power consumption, low operating cost and high sensitivity, thereby representing a realistic alternative to instrument-based systems.[1,2] To date, the fabrication of periodic dielectric materials, to achieve structure-based photonic sensors, has been attained through a range of disparate approaches. These techniques serve to achieve feature sizes that are comparable with the wavelength of the interrogating light, thereby resulting in reflection or transmittance of bright iridescent colours.[3,4] Lithographic techniques (in hard and soft materials), adapted from the semiconductor industry, such as e-beam lithography,[5] etching,[6] and nanoimprint lithography[7] have been used to produce high-fidelity nanostructures in 2D and 3D. Self-assembly of colloidal nanoparticles, self-ordering of cholesteric liquid crystals,[8] and sol gel chemistry[9] have also been used to generate responsive films which have found use as antireflection coatings and photonic crystal sensors (sensitive to pH, temperature, electric field, light, and a range of relevant biological analytes). [10–12] Using deposition methods to yield innovative material-based photonic structures may ultimately hinder potential fabrication form-factors, while top-down methods, focussing on complex 2D/3D photonic structures have been generally restricted to a limited number of materials (silicon, glass, metals, and diamond).

Direct Laser Writing (DLW) by two-photon polymerisation (2PP) relies on the simultaneous absorption of two photons of light to excite an initiator molecule. During the 2PP process, the beam of a near-IR femtosecond laser (780 nm) is focused into a highly defined 'spot', known as a volume element (voxel). This irradiation can provide enough energy to initiate polymerisation of a photosensitive material by absorption of two-photons, with reported axial resolution of ~300 nm and lateral resolution of ~100 nm.[13] DLW *via* 2PP has been used to great avail for the fast generation of extremely reproducible microscopic structures, and for the generation of complex hierarchical 3D photonic structures. In 2009, Farsari and co-workers demonstrated the potential of using the technique for the generation of three-dimensional photonic structures.[14] This approach, using organic-inorganic hybrid photoresists, has been extended in recent years to more complicated hierarchical architectures. This enables the generation of bioinspired structural coloration, mimicking the lamella on the *Morpho peleides* butterfly wings. It allows for imitation of naturally occurring photonic arrays, such as periodic microspheres, lunulae, and multilayer lamellae, among others.[15–17] More recently, the group of J. Wang exploited such high-resolution 3D fabrication combined with high temperature-induced irreversible shrinkage (at 450 °C) of a commercially available photoresist (IP-Dip) to generate 12 repeat-layer scaffolds.[18] Upon heating, different degrees of shrinking resulted in a range of different lattice constants, which correspond to a wide variation of reflected colours. Moreover, they extended this approach to confer structural coloration onto 3D microscopic structures. Subsequently, they have used a modification of another proprietary photoresist, based on isobornyl-acrylate (Veroclear) to generate a shape memory polymer. In this instance, by heating above the glass transition

temperature, they demonstrate the ability to apply a load to the structures which can be used to reversibly negate the photonic response.[19]

To date, many 2PP structures in the literature use vendor-purchased photoresists, with high concentrations of monomers and crosslinkers, to generate high-resolution, rigid structures.[20,21] While the generation of optical components from hard plastics serves an important purpose, there exists a world of additional potential which can be achieved through microfabrication in stimuli-responsive materials.[22,23] Using this approach, it is also possible to generate structures which possess controllable nanoscale photonic behaviour with programmable hierarchical structures, to create a new generation of responsive photonics. In this regard, herein we demonstrate the first example of DLW-fabricated photonic arrays capable of reversible response to vapours (isopropanol, ethanol, water) under atmospheric conditions. This is achieved by combining 3D soft-lithography fabrication technologies with soft, stimuli-responsive polymers. The method described here can now be expanded to a wide range of soft polymer structures and stimuli that could generate a (reversible) expansion of the polymer structure (e.g. vapours, local chemical environment, temperature, light, and electric field).

Results and discussion

The role of solvent and solvent concentration in pre-polymer photoresists is a critical aspect of DLW, where structures are fabricated in a voxel-by-voxel manner. It is therefore essential to achieve efficient polymerisation and crosslinking in each voxel, and most often this paramount requirement results in photoresists with high concentrations of liquid monomers (or minimal solvent content) and multifunctional crosslinkers.[24–26] While these ensure high fidelity structures, with high resolution, they often result in highly crosslinked materials which render the materials unsuitable for the efficient inclusion of a stimuli-response.[20] In the past three years we have started to see responsive hydrogel actuators being introduced to DLW, but their library remains relatively limited.[27–29] Herein, using an ionic liquid (IL) as cosolvent, we have achieved successful solubilisation of all photoresist components with high solvent content (>40 wt. %). **Figure 1a** depicts the use of a tetrabutyl phosphonium chloride IL to allow for successful solubilisation of the acrylamide monomer, pentaerythritol triacrylate crosslinker, in addition to the 7-(Diethylamino)-3-(2-thienyl)coumarin photo-initiator, for DLW fabrication of high fidelity ionogel structures. The use of ILs as photoresist solvents for DLW is ideal for the fabrication of soft ionogel structures and can be applied to a wide range of monomers and crosslinkers used for the fabrication of soft responsive hydrogels at the macroscale. The inherited tunability of ILs to yield desired solvation properties has led to them being known as designer solvents and their use as 'greener' alternatives for various synthetic processes.[30]

Herein we explore the advantages of 2PP-enabled fabrication of soft hydrophilic microstructures with sub-micron features, by fabricating periodic 2D grid structures that display structural
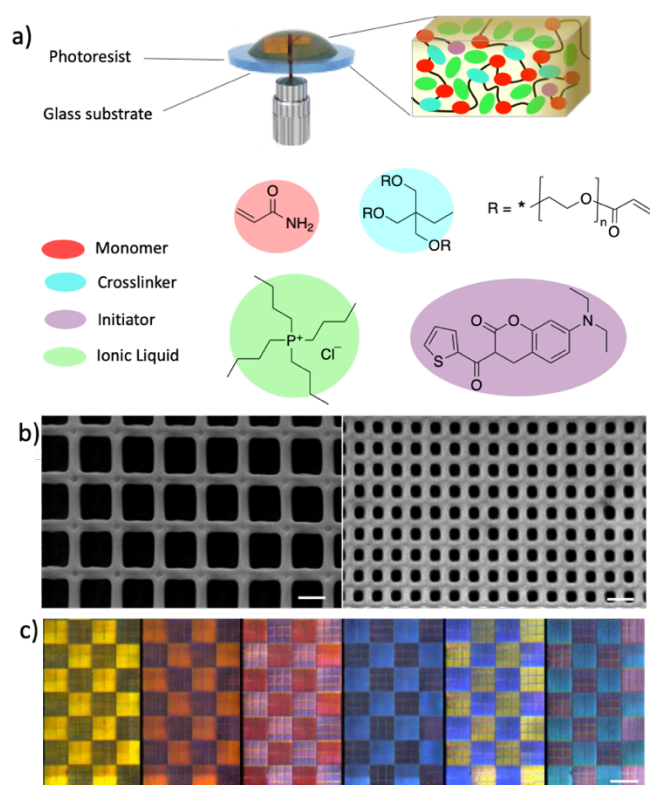

Fig. 1 Direct laser writing for the fabrication of responsive photonic structures a) Schematic of the direct laser writing process and photoresist composition; All structures were fabricated in the oil immersion configuration; SEM images (b) and angle-dependent optical microscopy images (c) of periodic photonic structures fabricated through alternate fabrication of two types of square arrays, creating a checkerboard pattern. Scale bar represents 2.0 μm in b) and 200 μm in c).

colour controlled by the geometry of the repeating unit (**Figure 1b** and **c**) and the angle of the observer. Through the use of Finite Difference Time Domain (FDTD) (SI, section 1.5) analysis, prediction of transmission spectra for suitable designs and simulation of swelling-induced size changes can be achieved. For the purpose of this work, we concentrate on a single set of geometries (**Figure 2a**), comprising a periodic grid of 2.75 μm by 2.75 μm (a), line width (d) of 0.5 μm, and varying heights h (1.5 μm, 2.0 μm, 2.5 μm, 3.0 μm and 3.5 μm). The effect of varying each of these parameters is shown in the simulations presented in Figure S4. For optical measurements, each grid array covered a total area of 290 μm by 290 μm, achieved through sequential fabrication of a 5 x 5 array of 58 μm x 58 μm repeating units. The corresponding optical and scanning electron microscope (SEM) images (Fig S5-S8) show the homogeneity of the features and the fidelity of the overall array with respect to the CAD design. The fabricated lines of ~0.5 μm in width represent the smallest features achieved in crosslinked acrylamide copolymer fabricated to date via 2PP. This achievement represents a significant step for the generation soft hydrogel materials with sub-micron features, and the ability to incorporate stimuli response into microscopic DLW-fabricated structures. The optical microscope images of the arrays shown in **Figure 2b**, demonstrate the vibrant transmitted colours and the dramatic changes seen with increasing structure height. This is supported by the simulations and measured transmission spectra shown in **Figure 2c**. Details of the transmission measurements can be found in SI Sections 1.4 and 3.1.
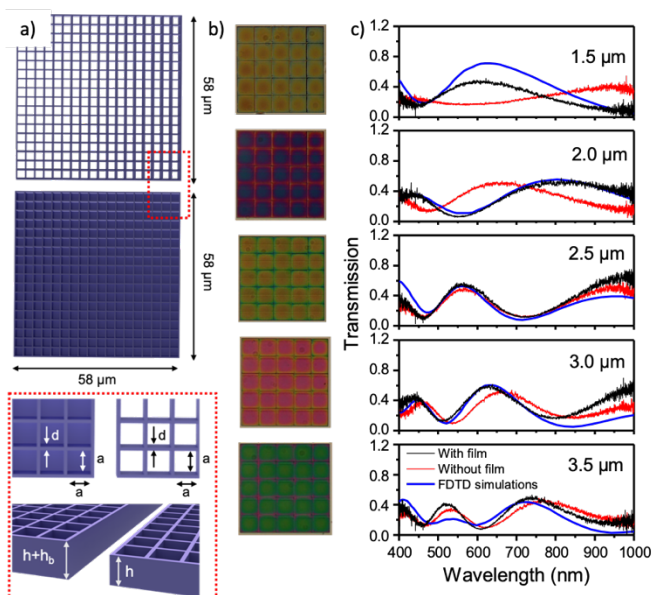
Fig. 2 Design, images, and transmission spectra of photonic grid arrays. a) The photonic structures were achieved through sequential fabrication of 58 μm × 58 μm repeating units of designed line width (d), height (h) and distance between parallel lines (a). For improved grid height control during the DLW fabrication process, a second structure iteration contained a thin film underneath the photonic structures, of a nominated height (h_b). b) Transmission optical microscopy images of the fabricated structures with the film underneath, where the designed height of the grid structure is (top to bottom) 1.5 μm, 2.0 μm, 2.5 μm, 3.0 μm and 3.5 μm, respectively. c) Corresponding measured transmission spectra with and without the under-structure film, and comparison with FDTD simulated spectra for grid structures of designed dimensions (a, d, h).

In DLW, discrepancies in the design and fabricated grid heights can often be caused by minor variations in interface values between the substrate and monomeric photoresist (Figures S4, S7, S11-S13). Inclusion of a thin film (h_b = 1.0 μm, Fig 2a) underneath the structures, serves to absorb any variation in heights (Figure S1), resulting in greater homogeneity across structures and better agreement with simulated spectra, as shown in **Figure 2c** and Figure S11. From the simulations, presented in greater detail in Figure S4, it is clear that variation in square size (here represented by a, the distance between two neighbouring lines) has only a minimal impact on peak positions in the predicted spectrum. Variation of height (h) and line width (d), however, are seen to have a dramatic impact on the position of main spectral bands and the relative intensity number of resulting peaks and troughs.

As the material used for these microstructures is based on the hydrophilic acrylamide monomer, they have the ability to swell in the presence of polar solvents in the liquid and vapour state. To interrogate the possibility of employing this behaviour to yield a measurable visual response upon exposure to different vapours, we developed a simple bubbling system, in which gas vapours were transported using dry air as a carrier, through a flow-in flow-out quartz cell. By initially exposing the samples to a flow of compressed dry air, it was possible to eliminate any contributions from relative humidity changes in the environment. Capturing images and transmission spectra using a bespoke optical system (Figure S2), the optical response of the arrays was observed in real time. To study the spectral diversity of vapor responses of the photonic structures, three model vapours were selected, namely isopropanol, ethanol, and water. The dynamic responses of arrays upon exposure to these vapours over the whole visible spectrum is exemplified in **Fig. 3**
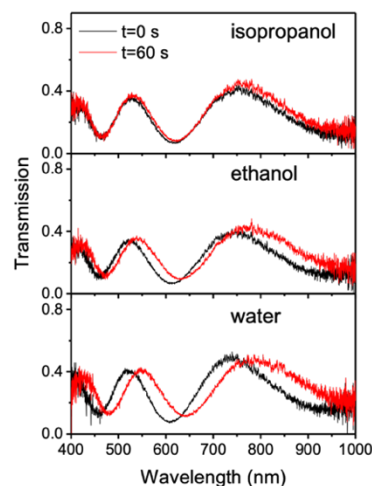

Fig. 3 Transmission spectra of the photonic structures of designed height h = 3.5 μm with film, before (black) and after 1 min in the presence of solvent vapours (IPA – top; ethanol – middle and water – bottom) where the gas vapours were transported using dry air at a flow rate of 1L/min.

for a 3.5 μm tall array. The observed red shift in the transmission spectrum increased with the polarity of solvent (isopropanol < ethanol < water) and was greater for higher flow rate of the exposing solvent (Fig. S15). The redshift of the spectral peaks indicates increased dimensions of the grid linewidth and height (Fig. S4 and S17) and can be used to accurately differentiate the response from a mere influence of modulating ambient refractive index. It is also noteworthy that, while the presence of a thin base layer underneath the grids served to produce greater homogeneity of height and colour, the arrays fabricated without this layer exhibit larger spectral shifts (Fig. S16). This can be attributed to a greater symmetry of expansion, upon introduction of the underlying film, by overcoming the restriction caused by direct attachment of the grid to the substrate.

The fast and notable response gave the opportunity to follow the spectral changes in real time. An example of such a response to water vapour is shown **Figure 4.**
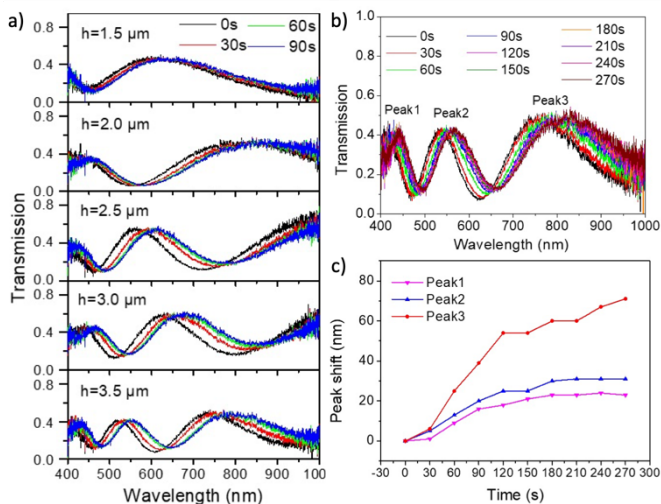

Fig. 4 a) Transmission spectra of the photonic structures of different designed heights (top to bottom: 1.5 μm, 2.0 μm, 2.5 μm, 3.0 μm and 3.5 μm) at different time points under a 1L/min flow of water vapour b) Transmission spectra of a nominated array of h =3.5 μm in the presence of water vapours over time (0-270s). c) Data extracted from b showing the peak shift over time in the presence of water vapours (dry air carrier flow rate was 0.5L/min) for the three maxima. Integration time was set to 3.94s.
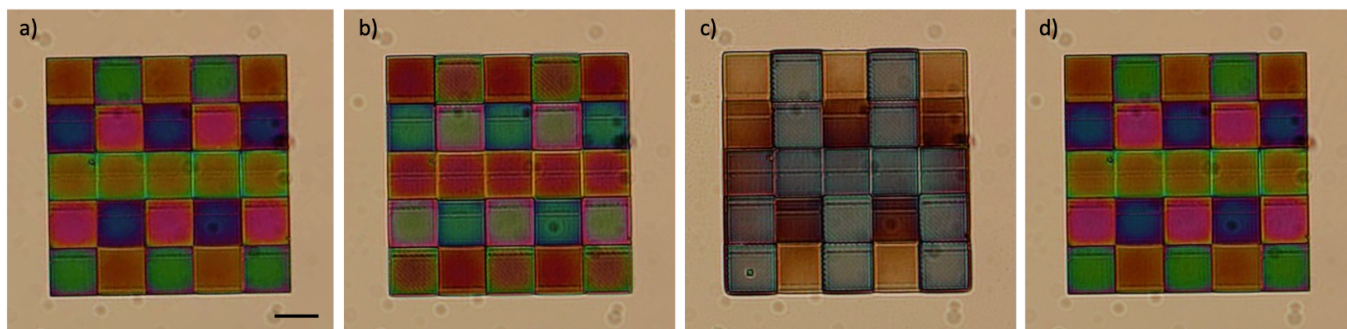
Fig. 5 a) Transmittance optical image of a grid array where each column is composed of five repeating units of different heights (left column, the designed height of the grid structure is (top to bottom) 1.5 µm, 2.0 µm, 2.5 µm, 3.0 µm and 3.5 µm, respectively). b) the same array upon exposure to water vapours for approximately 20 s (video S1. t = 0:26) and c) upon saturation with water vapours for approximately 88 s (video S1. t = 1:34). d) the array returns to its original colour 4 s after the gas flow is stopped. A flow rate of 1L/min was used for the dry air carrier gas. Scale bar represents 50 µm.

Figure 4a shows a significant red shift in the spectral bands which is observed upon coming in contact with water vapour. The response increases with respective height of the arrays. The greatest shift in wavelength in all cases, combined with a significant peak broadening, is observed for the longest wavelength band in the transmittance spectrum of each array (**Fig. 4c**). The transmission spectra, in the presence of the water vapour for a flow rate of 1 L/min, can be simulated for a 5% to 7.5% expansion of the linewidth and height (Fig. S16).

Fascinated by the dynamic response of different arrays, we sought to fabricate a rudimentary pixelated sensor, in which the different colours are achieved using different height arrays (**Figure 5**). Five different heights, from 1.5 to 3.5 µm, were woven sequentially up and down, creating a reoccurring pattern of orange (1.5 µm), blue (2.0 µm), red (2.5 µm), pink (3.0 µm), and green (3.5 µm). In the presence of water vapour, the colours are seen to rapidly change, shown in Figure 5b, with the most dramatic response visible for the higher arrays. Upon accumulating large amounts of water, which serves to fully hydrate the structure and to condense in the voids, the visible photonic response of the thinner arrays is completely disrupted, revealing a pattern created only by the taller arrays (**Figure 5c**). SEM images of this array, in Figure S18, serve as a useful comparator. Within 4 seconds of ceasing the water vapour flow, the initial state fully returns (**Figure 5d**). This can be used, quite impressively, to generate appearing and disappearing motifs whose colour and responsiveness can be pre-programmed into the fabricated design. The resulting spectral differences can be further explored to analyse the vapor-response diversity of the sensor, by employing Principal Components Analysis (PCA) and Hierarchical Cluster Analysis (HCA) tools. These approaches are extremely beneficial to look at clustering based on the nature of diverse spectral features produced by exposures of the sensor to different vapours and concentrations.

Additionally, more complex 3D structures can also be realised, showing that the material reported here is suitable for 2PP-fabrication of self-supporting 3-dimensional periodic structure. The example shown here is a woodpile structure which contains a total of 15 sequentially layered lines, with submicron features (Fig. S9).

Conclusions

A soft, hydrogel material, was fabricated into a responsive photonic array with sub-micron features. This was made possible through the use of an appropriate ionic liquid co-solvent, which allowed for solubility of all components and subsequent fabrication using DLW. The resulting periodic structures swell reversibly in the presence of solvent vapours to generate a measurable optical response which is determined by the polarity of the solvent. The working principle is explained using FDTD analysis, where the experimental colour and wavelength changes are correlated with changes in the dimensions of the structures in real time. The principle presented herein can be applied to a wide range of polymer formulations (including stimuli-responsive hydrogels) and structural designs, to achieve functional photonic structures that will grant the desired spectral changes in response to the stimulus of interest.

Conflicts of interest

There are no conflicts to declare.

Acknowledgements

Notes and references

1   C. Fenzl, T. Hirsch and O. S. Wolfbeis, *Angew. Chemie - Int. Ed.*, 2014, **53**, 3318–3335.

2   R. A. Potyrailo, N. Karker, M. A. Carpenter and A. Minnick, *J. Opt.*, 2018, **20**, 024006.

3   S. Daqiqeh Rezaei, Z. Dong, J. You En Chan, J. Trisno, R. J. H. Ng, Q. Ruan, C.-W. Qiu, N. A. Mortensen and J. K. W. Yang, *ACS Photonics*, 2021, **8**, 18–33.

4   R. A. Potyrailo, R. K. Bonam, J. G. Hartley, T. A. Starkey, P. Vukusic, M. Vasudev, T. Bunning, R. R. Naik, Z. Tang, M. A. Palacios, M. Larsen, L. A. Le Tarte, J. C. Grande, S. Zhong and T. Deng, *Nat. Commun.*, 2015, **6**, 7959.

5   S. Daqiqeh Rezaei, J. Ho, T. Wang, S. Ramakrishna and J. K. W. Yang, *Nano Lett.*, 2020, **20**, 4422–4429.

6   E. D. Le Boulbar, C. J. Lewins, D. W. E. Allsopp, C. R. Bowen and P. A. Shields, *Microelectron. Eng.*, 2016, **153**, 132–136.

7   C. Delaney, N. Geoghegan, H. Ibrahim, M. O'Loughlin, B. Rodriguez, L. Florea and S. Kelleher, *ACS Appl. Polym. Mater.*, **2**, 3632–3641.

8   M. Pozo, C. Delaney, C. Bastiaansen, D. Diamond, A. Schenning and L. Florea, *ACS Nano*, 2020, **14**, 9832–9839.

9   R. M. Almeida, L. M. Fortes and M. Clara Gonçalves, *Opt. Mater. (Amst).*, 2011, **33**, 1867–1871.

10 A. J. J. Kragt, R. C. G. M. Loonen, D. J. Broer, M. G. Debije and A. P. H. J. Schenning, *J. Polym. Sci.*, , DOI:https://doi.org/10.1002/pol.20210008.

11 A. A. F. Froyen, M. Wübbenhorst, D. Liu and A. P. H. J. Schenning, *Adv. Electron. Mater.*, 2021, **7**, 2000958.

12 A. Belmonte, M. Pilz da Cunha, K. Nickmans and A. P. H. J. Schenning, *Adv. Opt. Mater.*, 2020, **8**, 2000054.

13 L. Zheng, K. Kurselis, A. El-Tamer, U. Hinze, C. Reinhardt, L. Overmeyer and B. Chichkov, *Nanoscale Res. Lett.*, 2019, **14**, 134.

14 M. Malinauskas, A. Gaidukevičiūtė, V. Purlys, A. Žukauskas, I. Sakellari, E. Kabouraki, A. Candiani, D. Gray, S. Pissadakis, R. Gadonas, A. Piskarskas, C. Fotakis, M. Vamvakaki and M. Farsari, *Metamaterials*, 2011, **5**, 135–140.

15 G. Zyla, A. Kovalev, M. Grafen, E. L. Gurevich, C. Esen, A. Ostendorf and S. Gorb, *Sci. Rep.*, 2017, **7**, 1–9.

16 G. Zyla, A. Kovalev, E. L. Gurevich, C. Esen, Y. Liu, Y. Lu, S. Gorb and A. Ostendorf, *Appl. Phys. A*, 2020, **126**, 740.

17 G. Zyla, A. Kovalev, S. Heisterkamp, C. Esen, E. L. Gurevich, S. Gorb and A. Ostendorf, *Opt. Mater. Express*, 2019, **9**, 2630–2639.

18 Y. Liu, H. Wang, J. Ho, R. C. Ng, R. J. H. Ng, V. H. Hall-Chen, E. H. H. Koay, Z. Dong, H. Liu, C.-W. Qiu, J. R. Greer and J. K. W. Yang, *Nat. Commun.*, 2019, **10**, 4340.

19 W. Zhang, H. Wang, H. Wang, J. Y. E. Chan, H. Liu, B. Zhang, Y.-F. Zhang, K. Agarwal, X. Yang, A. S. Ranganath, H. Y. Low, Q. Ge and J. K. W. Yang, *Nat. Commun.*, 2021, **12**, 112.

20 M. Carlotti and V. Mattoli, *Small*, 2019, **15**, 1902687.

21 A. K. Nguyen and R. J. Narayan, *Mater. Today*, 2017, **20**, 314–322.

22 D. Gräfe, S. L. Walden, J. Blinco, M. Wegener, E. Blasco and C. Barner-Kowollik, *Angew. Chemie Int. Ed.*, 2020, **59**, 6330–6340.

23 A. Tudor, C. Delaney, H. Zhang, A. J. Thompson, V. F. Curto, G.-Z. Yang, M. J. Higgins, D. Diamond and L. Florea, *Mater. Today*, 2018, **21**, 807–816.

24 N. Buch-Månson, A. Spangenberg, L. P. C. Gomez, J. P. Malval, O. Soppera and K. L. Martinez, *Sci. Rep.*, 2017, **7**, 1–9.

25 A. Marino, G. Ciofani, C. Filippeschi, M. Pellegrino, M. Pellegrini, P. Orsini, M. Pasqualetti, V. Mattoli and B. Mazzolai, *ACS Appl. Mater. Interfaces*, 2013, **5**, 13012–13021.

26 D. H. Kim, P. Kim, K. Y. Suh, S. K. Choi, S. H. Lee and B. Kim, *Annu. Int. Conf. IEEE Eng. Med. Biol. - Proc.*, 2005, **7 VOLS**, 4091–4094.

27 M. Hippler, E. Blasco, J. Qu, M. Tanaka, C. Barner-Kowollik, M. Wegener and M. Bastmeyer, *Nat. Commun.*, 2019, **10**, 232.

28 D. Jin, Q. Chen, T.-Y. Huang, J. Huang, L. Zhang and H. Duan, *Mater. Today*, 2020, **32**, 19–25.

29 Y.-L. Zhang, Y. Tian, H. Wang, Z.-C. Ma, D.-D. Han, L.-G. Niu, Q.-D. Chen and H.-B. Sun, *ACS Nano*, 2019, **13**, 4041–4048.

30 L. C. Tomé and D. Mecerreyes, *J. Phys. Chem. B*, 2020, **124**, 8465–8478.

Supporting Information

Direct laser writing of vapour-responsive photonic arrays

Colm Delaney,[a†] Jing Qian,[b†], Xia Zhang [b], Radislav Potyrailo[c], A. Louise Bradley[b] and Larisa Florea[a*]*

[a]*School of Chemistry & AMBER, the SFI Research Centre for Advanced Materials and BioEngineering Research, Trinity College Dublin, Dublin 2, Ireland*

[b]*School of Physics and AMBER, Trinity College Dublin, College Green, Dublin 2, Ireland*

[c]*General Electric Research, Niskayuna, NY, USA*

Email: floreal@tcd.ie

Table of Contents

1. Materials and Methods

1.1. Materials

Tetrabutyl phosphonium chloride ($[P_{4,4,4,4}][Cl]$), 80% in water was obtained from TCI, Japan. Acrylamide (Am) 98%, trimethylolpropane ethoxylate triacrylate ($M_w \sim 912$), and 3-(trimethoxysilyl) propyl methacrylate 98% were obtained from Sigma Aldrich, Ireland and used as received. 7-Diethylamino-3-thenoylcoumarin was obtained from Alpha Chemical, USA. All solvents including ethanol, isopropanol (IPA), propylene glycol methyl ether acetate (PGMEA), were high performance liquid chromatography grade (HPLC) purchased in anhydrous form, from Sigma Aldrich and used without further purification. Table S1 shows the photoresist composition used for the fabrication of photonic structures.

Table S1: Acrylamide (Am) based photoresist which used $[P_{4,4,4,4}][Cl]$ as cosolvent and 24 mol % trimethylolpropane ethoxylate triacrylate (TMPET) crosslinker.

Chemical	Molecular weight (g/mol)	Amount (mg)	Moles (mmol)	Mole % (in relation to Am)	wt %
Acrylamide (Am)	71.08	205	2.81	100.0	14.4
trimethylolpropane ethoxylate triacrylate (TMPET)	912	610	0.66	24	43
7-Diethylamino-3-thenoylcoumarin (DEATC)	327.39	4.1	0.012	0.42	0.3
Tetrabutylphosphonium chloride $[P_{4,4,4,4}][Cl]$ 80% solution	294.88	600	1.62	-	42.3

1.2. Structure fabrication by direct laser writing

Direct Laser Writing by two-photon polymerisation was performed on a Nanoscribe GT Photonic Professional system (Nanoscribe GmbH). This system uses a 170 mW laser operating at 780 nm. All structures were fabricated in the oil immersion configuration using a 63X immersion objective (Zeiss, Plan Apochromat). Substrates used for DLW were high precision glass substrates No. 1.5 (tol. ± 5 μm) with an accurate thickness of 170 μm ± 5 μm, purchased from Thermo Fisher Scientific. A drop of the unpolymerised photoresist was placed in the centre of the glass coverslip, while a drop of oil (Zeiss Immersol 518F) was placed in the centre of the glass substrate on the opposite side. Following a successful optimisation process, all structures were fabricated using the same parameters (50% laser power, 25 mW and 10000 μm/s scanning speed.)

To ensure covalent attachment of the fabricated structures to the glass substrate, the glass coverslips were treated using a silanisation procedure.[1] After fabrication, the structures were rinsed with isopropanol and dried under nitrogen.

1.3. Structure design

The design of the structures consisted of grid structures with a range of dimensions (line width, hole size and thickness). The samples used for vapour analysis consisted of a grid

structure designed from repeating squares of 2.75 μm by 2.75 μm (*a*), line width (*d*) of 0.5 μm of five different heights h (1.5 μm, 2.0 μm, 2.5 μm, 3.0 μm and 3.5 μm), as shown in Figure S1. For optical measurements, each grid array covered a total area of 290 μm by 290 μm, achieved through sequential fabrication of 58 μm x 58 μm repeating units. In order to compensate for errors in thickness arising from the position of the substrate/photoresist interface (± 0.5 μm), a second set of structures was designed by adding a 1 μm base layer underneath the grid structure, while keeping all other dimensions the same. This base layer ensured that any error in the structure height, due to errors in identifying the interface (Fig. S1D), were absorbed by the solid base. This means that the incremental variation in the height of the photonic grid (*h* = 1.5 μm, 2.0 μm, 2.5 μm, 3.0 μm and 3.5 μm, respectively) was kept constant.
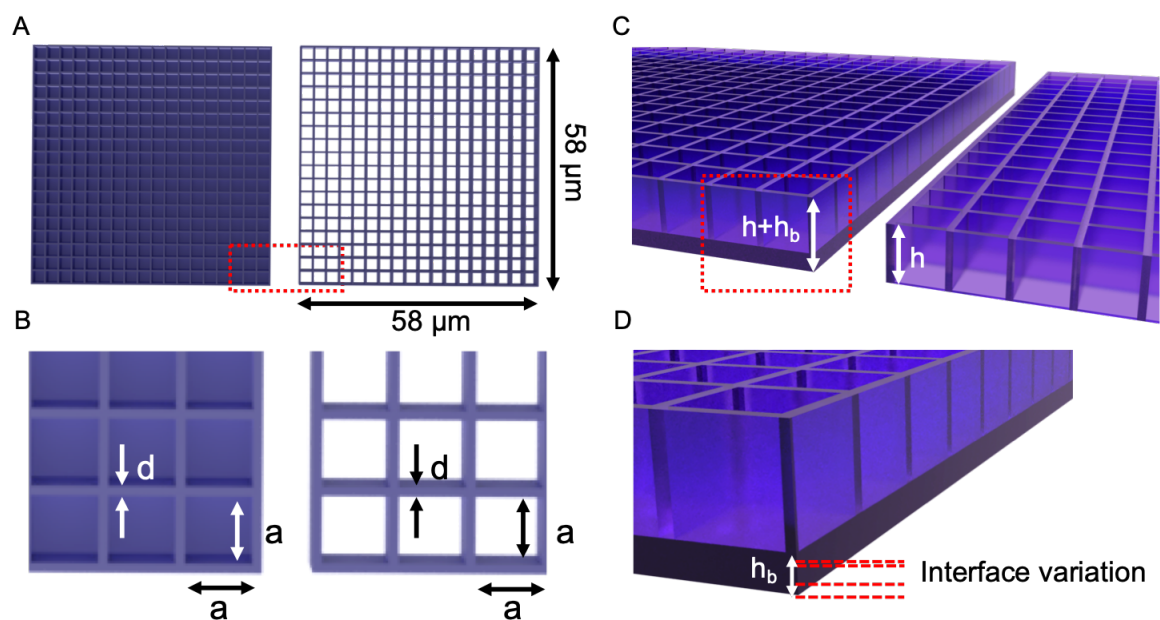

Figure S1: Top (A,B) and side view (C, D) of grid structure with and without the base layer. **A)** Top view of the 58 μm x 58 μm repeating grid structure with (left) and without (right) the 1 μm base layer. **B)** Top view detail showing the dimensions of the designed grids with (left) and without (right) the base layer; *a* = 2.75 μm; *d* = 0.5 μm; . **C)** Side view of the grid structure with (left) and without (right) the 1 μm base layer. h_b = 1 μm; *h* = 1.5 μm, 2.0 μm, 2.5 μm, 3.0 μm and 3.5 μm, respectively. **D)** Side view detail of the grid structure with base layer (h_B = 1 μm) showing its role in compensating for any variation in interface position, thereby ensuring a constant incremental variation in *h*.

1.4. Transmission measurement set-up with integrated bubbling system

Figure S2A shows the in-house customized transmission measurement setup which can then be integrated with the bubbling system, as shown in Figure S2B. In this configuration, the three-dimensional adjustable sample holder was fixed on an upper rotating stage, and the sample was illuminated with collimated white light via a fiber and 4X objective lens. The signal was collected by a 5X objective lens (NA=0.1), and the magnified image generated through a lens combination, which consists of a convex lens (focal length f1=25.4mm) and a 20X objective lens. Combined with the three-dimensional adjustable sample holder, an iris can be used to select an area of interest for measurement. The signal from the region of interest is passed through a beam-splitter to a fibre-coupled spectrometer and CCD camera, respectively. The samples were characterized under normal incidence light and with the zero-order transmission data presented in the manuscript. The change in transmission with viewing angle could also be measured by separately rotating the detection arm.
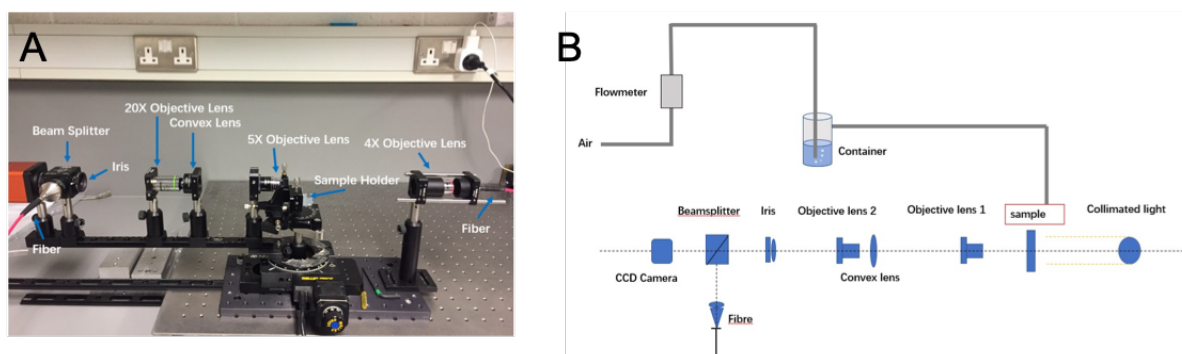

Figure S2. A) Image of the angle-resolved transmission setup. **B)** Schematic for integration of the bubbling system for vapour sensing into the optical setup.

1.5. Finite Difference Time Domain (FDTD) simulations

A commercial FDTD numerical simulation tool was used to simulate the transmission spectra of the designed grid structure and to investigate the influence of dimension changes on the transmission spectra. A refractive index of 1.5 was used over the full spectral range corresponding to the volume weighted solution refractive index with an error of ±0.03. The refractive index of acrylamide, trimethylolpropane ethoxylate triacrylate and tetrabutylphosphonium chloride are 1.46[2], 1.47[3], 1.5[4], respectively. The simulation setup for a 4×4 grid structure is shown in Figure S3. A plane wave source was used, located at 2 microns below the glass surface. PML boundary conditions were applied in x, y and z directions with a mesh size of 0.1×0.1×0.01 μm. A monitor recorded the transmitted signal 50 μm above the structure.
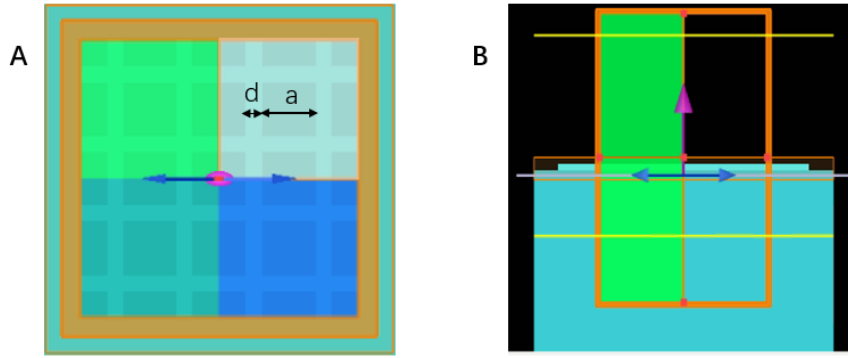
Figure S3. **A)** and **B)** show the top view and cross-section view of a 4 × 4 grid structure.

Figure S4 shows the effect of changing the line width (d), the structure height (h) and the size of the square (a) of a grid structure, on the transmission spectrum. It can be observed that changing the size of the square (a) from 1.00 μm to 3.5 μm, as shown in Figure S4A, has a less dramatic effect on the positions of the transmission bands compared to changes in the line width d (Figure S4B and C) and grid height h (Figure S4D). The coloured squares shown in Figure S3A indicated the CIE colours calculated from the spectra, with little change in expected colour observed over the range. The FDTD simulations reveal that line width changes ($d = 0.5$ μm to 0.7 μm, while keeping the height constant) and grid height changes ($h = 1.5$ μm to 4 μm, while keeping the line width constant) can generate a significant peak red shift in the transmission spectrum, accompanied by changes in the relative intensity of the transmission bands.

As the grid structures are used for vapour sensing, FDTD simulations were also used to simulate the effect of changes in the refractive index of the ambient environment on the transmission spectra (Figure S4E). Increased ambient refractive index, $RI_{(ambient)}$, over the range 1 to 1.2 results in a blue shift of the spectral peaks. Figure S4F shows that any decrease in the refractive index of the grid, $RI_{(polymer)}$, will also result in a blueshift of the spectral peaks.
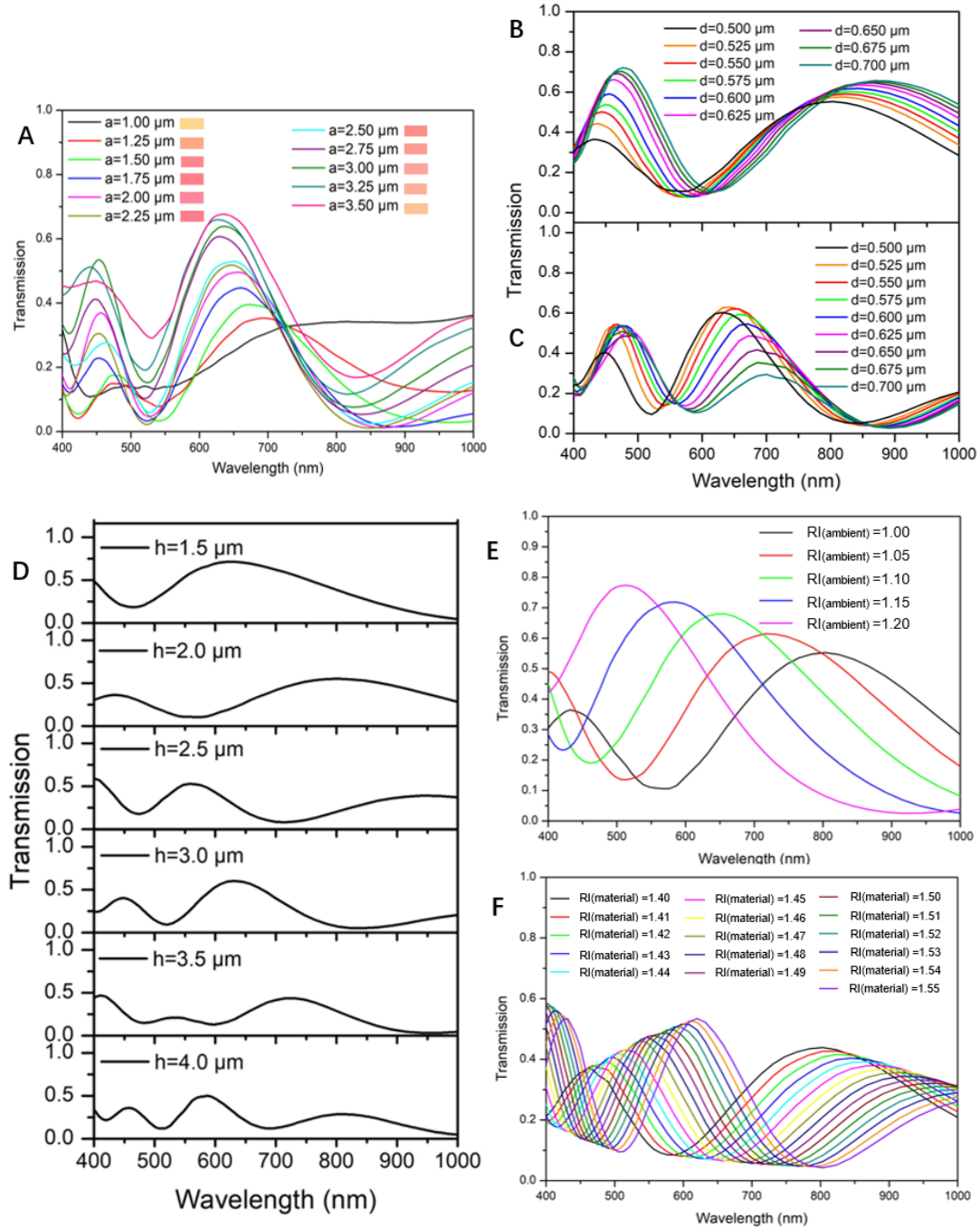
Figure S4. Simulated transmission spectra of a grid structure, generating by varying the grid dimensions (size of repeating square (*a*), line width (*d*) and the structure height (*h*)) and the refractive index of the gas environment or polymer structure. **A)** Transmission spectra for different values of *a*, when *d*=0.5 μm and *h*=3.0 μm. Inset colours represent the CIE coordinates; **B)** and **C)** Transmission spectra for different line width (*d*=0.5 μm to 0.7 μm) when square size (*a*) and structure height (*h*) are kept constant (*a*=2.75 μm, *h*=2.0 μm and 3.0 μm); **D)** Transmission spectra for different structure heights (*h*=1.5 μm to 4 μm, in 0.5 μm increments) when square size (*a*) and line width (*d*) are kept constant (*a*=2.75 μm and *d*=0.5 μm). **E)** Transmission spectra changes generated as a result of changing the refractive index of the ambient environment (RI $_{(ambient)}$ = 1 to 1.2, in 0.05 increments); **F)** Transmission spectra changes generated as a result of changing the refractive index of the polymer structure (from RI$_{(polymer)}$ = 1.4 to 1.55, in 0.01 increments).

2. Structure Characterisation

2.2. Optical microscopy

Following fabrication and development, structures were analysed using optical microscopy using an inverted ZEISS Axio Vert.A1 optical microscope. Optical microscope images below (Figure S5) show a typical grid structure covering an area of 290 μm × 290 μm, achieved through sequential fabrication of 58 μm × 58 μm repeating units.
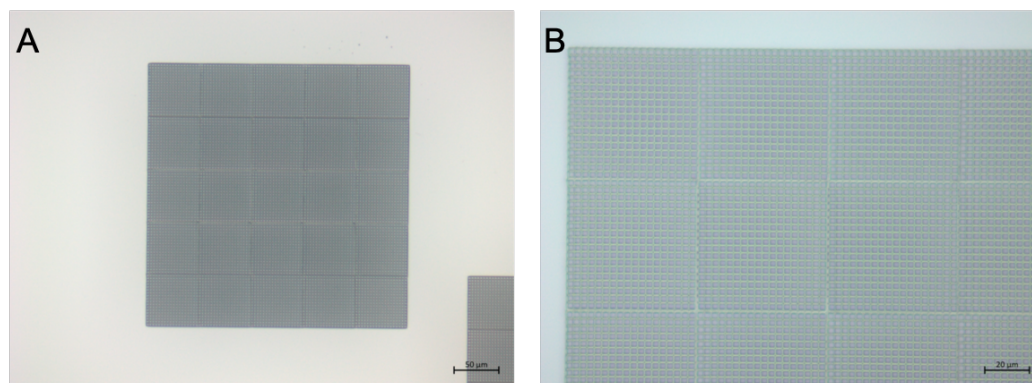

Figure S5. Optical microscope images at different magnification showing a typical grid structure (no base layer, $h = 3.5$ μm) covering an area of 290 μm by 290 μm, achieved through sequential fabrication of a 58 μm × 58 μm repeating unit.

2.3. Scanning electron microscopy

Scanning Electron Microscopy of the fabricated grid structures was carried out on a Zeiss Ultra Plus Scanning Electron Microscope, using an accelerating voltage of 5 kV. Prior to SEM imaging, the structures were coated with 30 nm Au-Pd layer using a Cressington Sputter Coater 208HR. Fig. S6-S8 show the SEM images of the five grid structures (no base layer) with heights of 1.5 μm, 2.0 μm, 2.5 μm, 3.0 μm and 3.5 μm, respectively.

Line width and square size for each grid structure were measured manually from top-down SEM using the measure tool in ImageJ. A minimum of six measurements were performed per fabricated grid to ensure a representative measurement. The average square, line width, and respective % errors were tabulated for each grid height (Figure S7F).

The designed versus experimentally measured square and line width dimensions (from SEM images) are listed in Fig. S7F. Compared to the designed dimensions, the error of the line width (d) is ~6%-20%, and the error of the square inner length (a) is ~2%-7% (Figure S7F). The error in structure height is mainly due to the automatic interface finder. During the direct laser writing process, the interface finder is set at -0.5 μm (0.5 μm below the substrate) to ensure correct identification of the photoresist/substrate interface. In the event of this not being this value, incorrect identification of the interface can result in fabrication starting above the surface, resulting in structure delamination during or after fabrication. Therefore, there will be

a maximum 0.5 μm mismatch between the designed and actual structure height. By comparing experimental transmission spectra with simulation spectra, shown in Fig. S13, the simulated height of each grid structure (h_{sim}) can be found (Fig. S7F). The grid samples with the smaller designed height (h=1.5 μm and h=2 μm) show the highest errors between experimental and design dimensions, as expected, since the interface finder compensation has a more dramatic effect on the structures with lower heights.
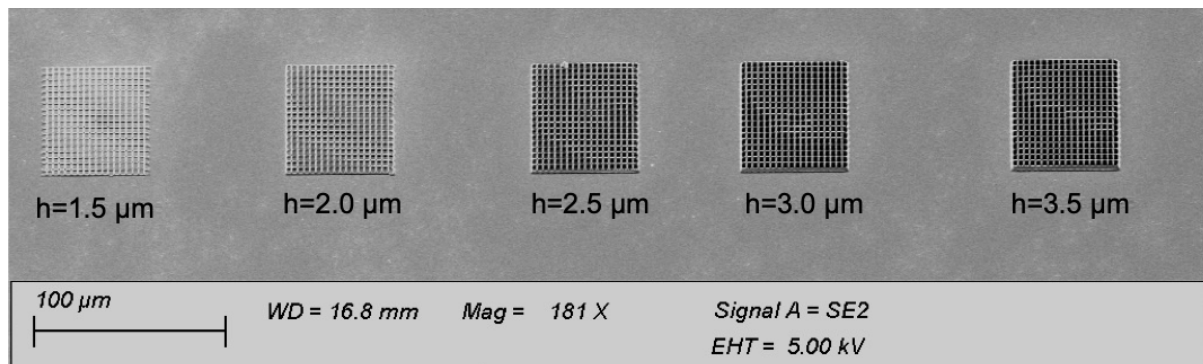

Figure S6. SEM images showing the 58 μm x 58 μm repetitive unit of the grid structure (no base layer) of different heights (1.5 μm, 2.0 μm, 2.5 μm, 3.0 μm and 3.5 μm).

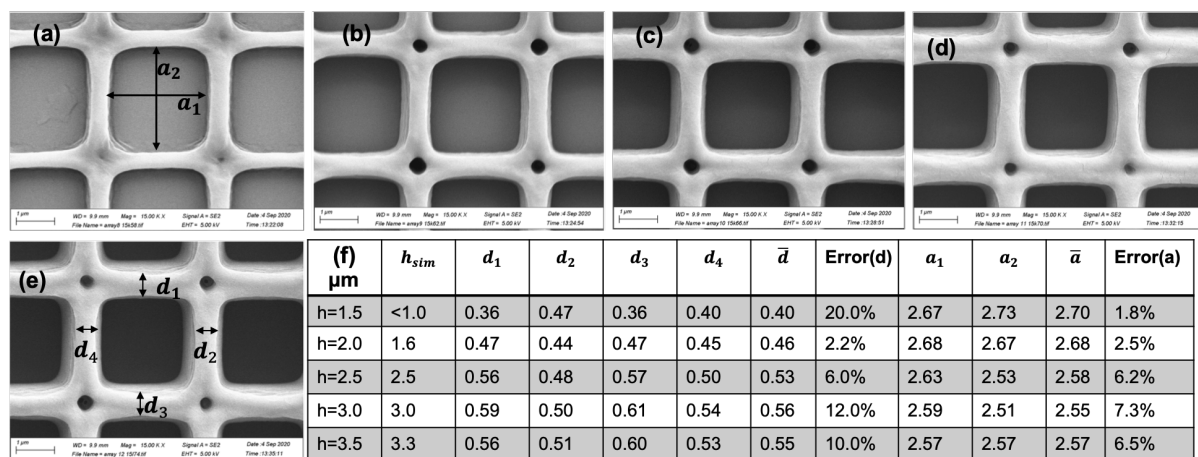| (f) μm	h_{sim}	d_1	d_2	d_3	d_4	$\bar{d}$	Error(d)	a_1	a_2	$\bar{a}$	Error(a)
h=1.5	<1.0	0.36	0.47	0.36	0.40	0.40	20.0%	2.67	2.73	2.70	1.8%
h=2.0	1.6	0.47	0.44	0.47	0.45	0.46	2.2%	2.68	2.67	2.68	2.5%
h=2.5	2.5	0.56	0.48	0.57	0.50	0.53	6.0%	2.63	2.53	2.58	6.2%
h=3.0	3.0	0.59	0.50	0.61	0.54	0.56	12.0%	2.59	2.51	2.55	7.3%
h=3.5	3.3	0.56	0.51	0.60	0.53	0.55	10.0%	2.57	2.57	2.57	6.5%

Figure S7. SEM images of the grid structure (no base layer) of different designed heights (*a*) 1.5 μm, (b) 2.0 μm, (c) 2.5 μm, (d) 3.0 μm, (e) 3.5 μm. (f) lists the measured line width for each structure (d_1, d_2, d_3, d_4), the average line width $\bar{d}$, representative length of the repeating square (a_1, a_1) and % error for line width and square length compared to design dimensions. h_{sim} represents the simulated structure height based on FDTD analysis of the transmission spectra of each of the grid structures.
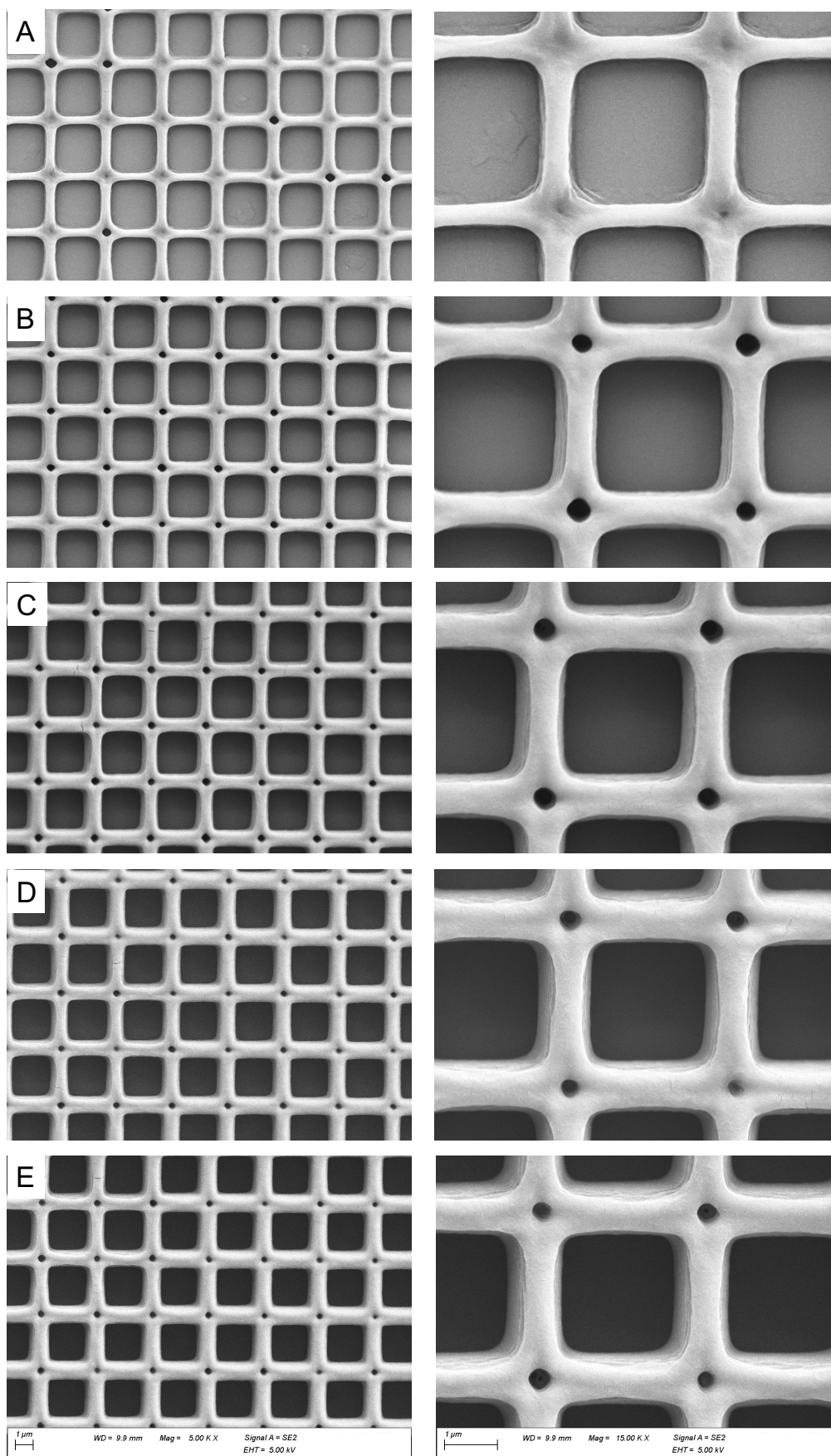
Figure S8. Representative SEM images at 5k and 15k magnification of the grid structures (no base layer) of different heights A) 1.5 µm, B) 2.0 µm, C) 2.5 µm, D) 3.0 µm and E) 3.5 µm. Scale bar represents 1 µm for all images.

An advantage of direct laser writing, is the ability to fabricate truly 3 dimensional structures with associated complexities of design. In this regard, 3-dimensional woodpile structures were also fabricated. The figure below shows an example of a layered woodpile structure which contains a total of 15 sequentially layered lines. It demonstrates the ability to achieve self-standing submicron features in this material (Fig. S9).
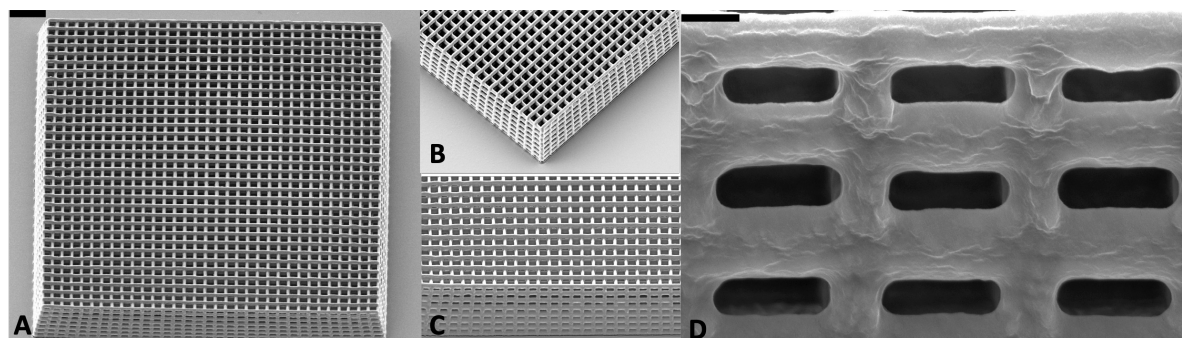

Figure S9. SEM images of 3-dimensional woodpile structure. The images shown in A) B) C) were taken at 30° tilt, scale bar represents 10 μm. The image shown in D) was taken at 40° tilt, scale bar represents 1 μm.

3. Transmission measurements

3.1. Angle resolved transmission spectra

The effect of changing the viewing angle on the transmission spectra was investigated using the in-house built angle-resolved setup introduced in section 1.4. Spectra for the grid structure with a height of 3.0 μm and no base layer is shown in Figure S10. Due to diffraction effects, the measured spectrum and observed colour changes for viewing angles greater than 4° become much weaker. All spectra shown in the manuscript correspond to the zero-order transmission with normally incident light.
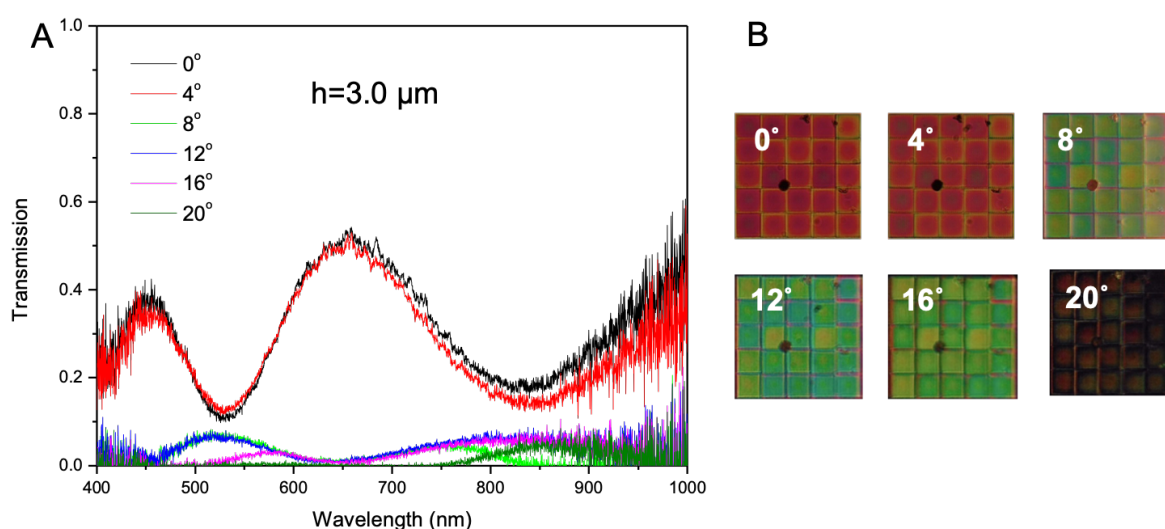

Figure S10. A) Transmission spectra of a 3.0 μm tall grid structure (without base layer) observed from different viewing angles; B) corresponding CCD images showing the colour in transmission observed at different viewing angles.

3.2. Zero-order transmission spectra for different grid structures

CCD images in Figure S11 show the colours of the grid samples of different height designs (1.5 μm, 2.0 μm, 2.5 μm, 3.0 μm and 3.5 μm) when viewed in transmission, with and without the underlying base layer. It is clear to observe that samples with different heights exhibit different structural colours. In the absence of a base layer, variation in the glass-photoresist interface results in a variation of grid height, and a resulting variation in observed colour across a given sample. This is consistent with the largest differences being seen for the lower grid height samples.
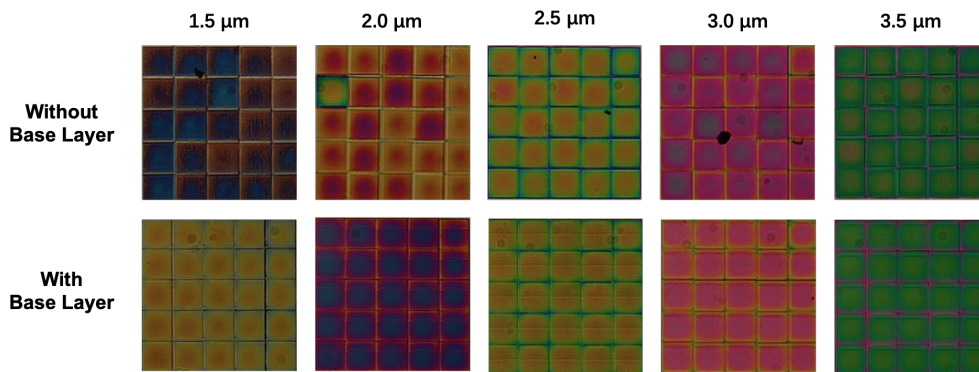

Figure S11. Comparison of CCD images of the grid structures of different heights viewed in transmission. Top row: structures fabricated without a base layer (L-R): 1.5 μm, 2.0 μm, 2.5 μm, 3.0 μm, 3.5 μm. Bottom Row: structures fabricated with a base layer (L-R): 1.5 μm, 2.0 μm, 2.5 μm, 3.0 μm, 3.5 μm.

Figure S12 (a) shows an example, where interface finder failed for one repeating unit, resulting in a different height and colour compared to the rest of the array.
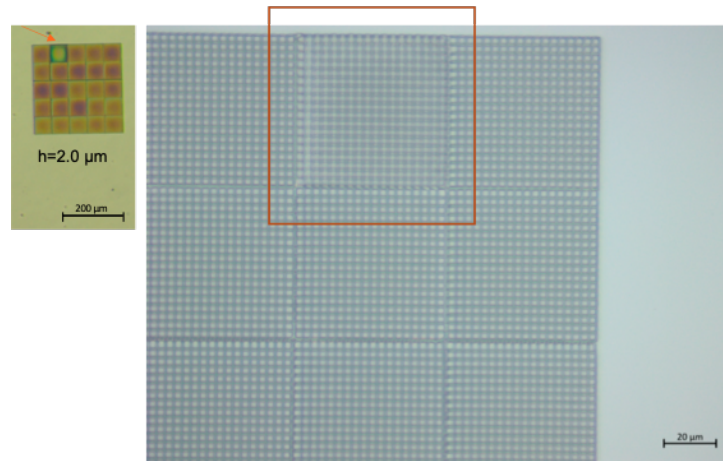

Figure S12. Optical microscopy images of a grid structure (2.0 μm designed height, without base layer) showing one of the fabricated repeating units (marked) at a higher height compared to the rest of the array. This is due to an error in the interface finder during the fabrication process, which results in a different colour.

Figure S13 provides measured transmission spectra for arrays with varying design heights (1.5 μm, 2.0 μm, 2.5 μm, 3.0 μm, 3.5 μm) in the absence of a base layer, compared with simulated spectra. Using the values of *a* and *d* obtained from the SEM images and table in Figure S7, the simulated grid height, h_{sim}, was adjusted to find the values which produce spectra corresponding to the experimental spectra. This can be used to confirm the discrepancy between the actual height and design height. As expected, the difference is more pronounced for the lower height structures. Greater agreement with the design value is observed for *h* above 2 μm.
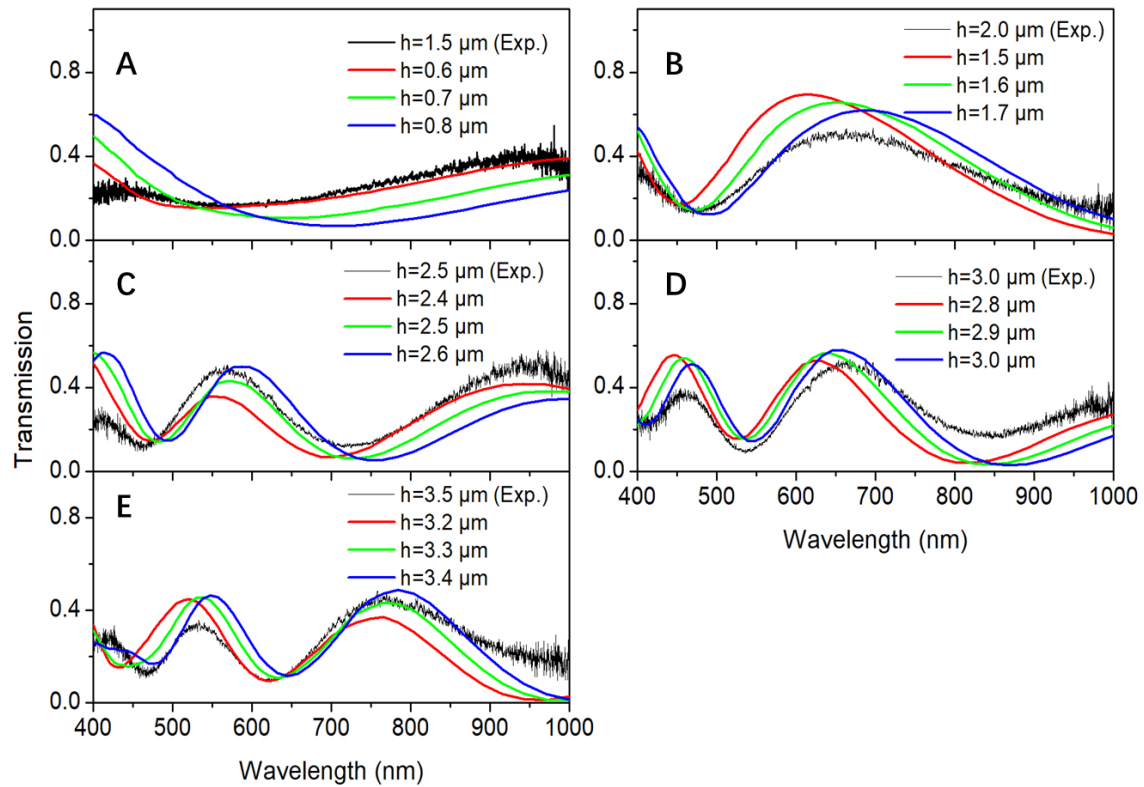

Figure S13. Measured transmission spectra for arrays without underlying film, directly compared with simulated spectra of varying height. A) when *d* = 0.4 μm and *a* = 2.7 μm. B) when *d* = 0.46 μm and *a* = 2.7 μm. C) when *d* = 0.53 μm and *a* = 2.6 μm. D) when *d* = 0.56 μm and *a* = 2.6 μm. E) when *d* = 0.7 μm and *a* = 2.6 μm.

Introduction of a 1 μm base layer underneath the photonic grid structure resulted in improved fidelity of the grid structure to the designed height, since any mismatch in the interface position will take place in the thin film base layer. This resulted in photonic structures showing more uniform structural colours compared to the structures without the 1 μm base layer, as seen in the bottom panels in Figure S11.
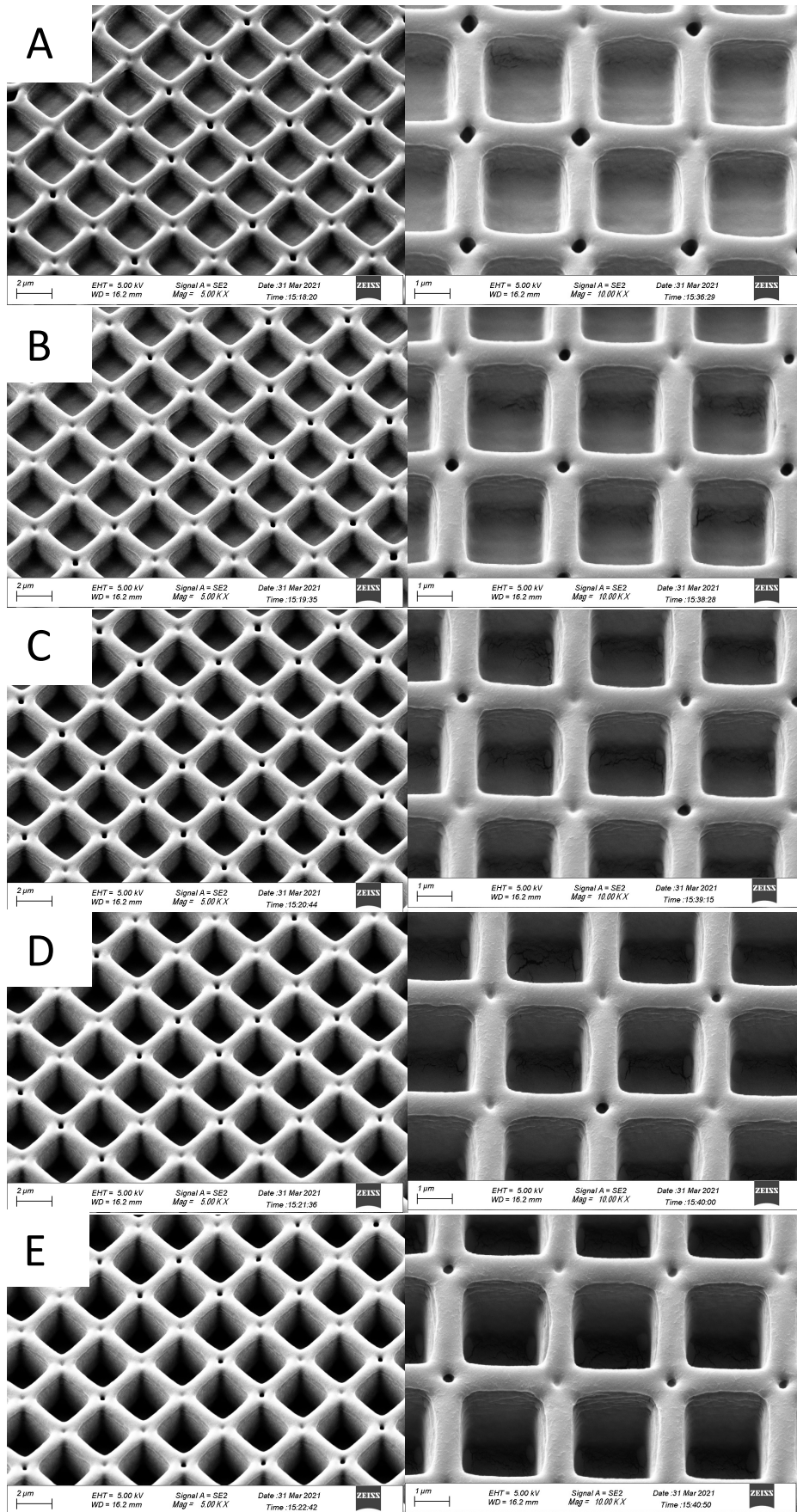
Figure S14. Tilt SEM images (30°) at 5k and 15k magnification of the grid structures (with 1 μm base layer of different design heights A) 1.5 μm, B) 2.0 μm, C) 2.5 μm, D) 3.0 μm and E) 3.5 μm.

Moreover, in order to verify the accuracy of structure height, the experimental spectra were compared with simulation results using the design parameters. The transmission spectra of samples with set dimension (a=2.75 μm, d=0.5 μm) and different thickness of 1.5 μm, 2.0 μm, 2.5 μm, 3.0 μm and 3.5 μm were calculated through FDTD simulations. From Fig. 2(c), the transmission spectra of the grid samples fabricated with the base layer are closer to the simulation results compared to the same grid designs fabricated without the base layer, especially for the thinner samples, as seen in Figure S13. Therefore, having a thin base layer represents a feasible option for reducing height errors, and improving design fidelity.

3.3 Solvent vapour sensing

Solvent vapour sensing was performed by measuring the transmission spectra of the samples using the in-house setup with integrated bubbling system. A sealed flow-in / flow-out quartz cell of dimensions 45 mm × 32.5 mm × 12.5 mm was designed to hold the sample. Dry air was used to dry the sample before each test to ensure that the sample was not affected by environmental humidity changes. A dry-air carrier gas was bubbled through solvents and was regulated using two Key Instruments FR2000 Series Variable Area Flow Meters (0.1 L/min → 0.5 L/min, and 0.4 L/min → 5 L/min respectively).

The spectral data in the presence of ethanol and water vapour is shown in Figure S15. Figure S15 (A and B) compare the responses to ethanol (red) and water vapour (blue) of a range of different height arrays. Focussing on a single array of design height 3.5 μm, Figure S15 C and D show that the solvent response is also dependent on the flowrate of the interrogating vapour, with greater red shifts seen for higher flowrates.
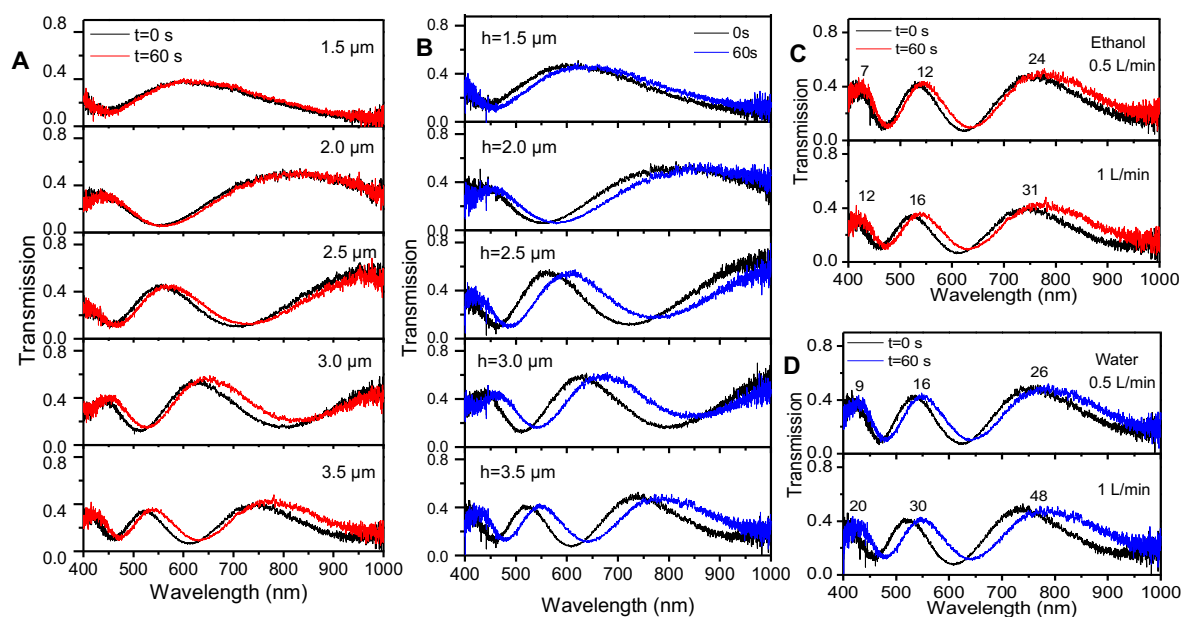

Figure S15. Spectra demonstrating the response of the arrays to ethanol and water vapour: A and B the different height arrays at a constant flow rate (1 L/min) of ethanol vapour and water vapour, respectively; C) and D) showing the effect of flowrate on a 3.5 μm tall array.

It is noted that, while addition of a stabilising base layer improves the homogeneity of height across an array, this can also serve to affect the response of the array. In the absence of the base layer, as can be seen by comparing Figure 3 in the main manuscript with Figure S16 below, a larger spectral shift can be achieved in response to vapours. This suggests that for a given volume expansion, the constrained expansion of the grid line which is covalently attached to the substrate in the absence of the underlying film, results in a greater increase in the grid height and consequently larger spectral shift. The grid lines on the base film could expand in both the horizontal and vertical directions. The simulations in Figure S4 show the greater influence of the change in grid height on the spectral shift.
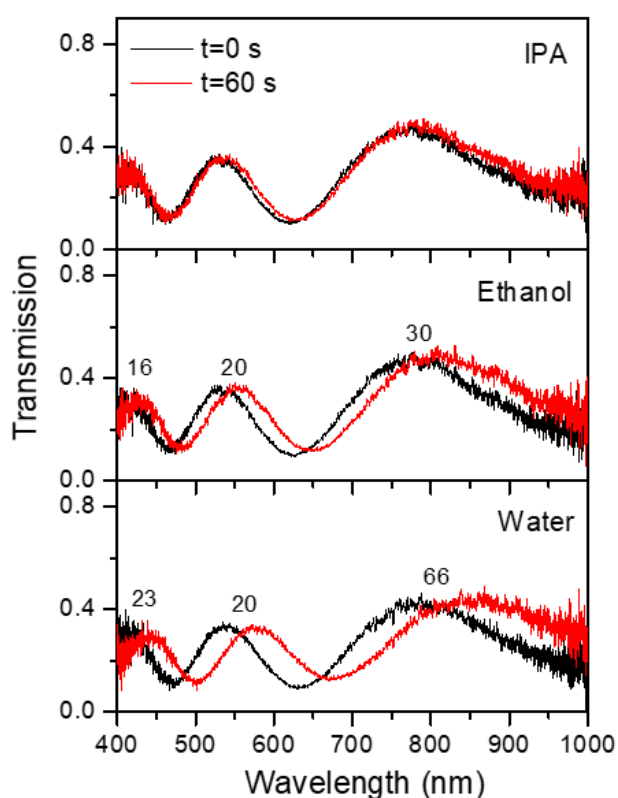

Figure S16. Transmission spectra of the photonic structures of designed height h = 3.5 μm without film, before (black) and after 1 min in the presence of solvent vapours (isopropanol– top; ethanol – middle and water – bottom) where the gas vapours were transported using dry air at a flow rate of 1L/min. Inset numbers represent the red shift of the peaks of the spectral bands.

To further understand the dynamic response of the polymeric grids, we turn to the measured transmission spectra before and after (90 seconds) the introduction of water vapour and compare this to FDTD simulations, shown in Figure S17. By assuming a symmetric swelling, in which the structure dimensions (d and h) expand by the same percentage, we can account for all spectral shifts (across all height arrays) by an expansion of just 5% - 7.5%. For the tallest structure, it is noted that the rectangular line cross-section does not give a good agreement with the amplitude of the transmission peak at ~ 525 nm. However, as the amplitude of the transmission is influenced by the cross-sectional geometry, we posit that using a trapezoidal

shape with values of $a = 2.6$ μm, $d = 0.65$ μm and $h = 3.3$ μm, a much better fit to the experimental spectra can be obtained, and can be used to give good agreement with the experimental spectra for the same expansion percentage. Using these parameters, and an expansion of 5% in d and h, an excellent fit to the data for the grid after water vapour exposure is also obtained.
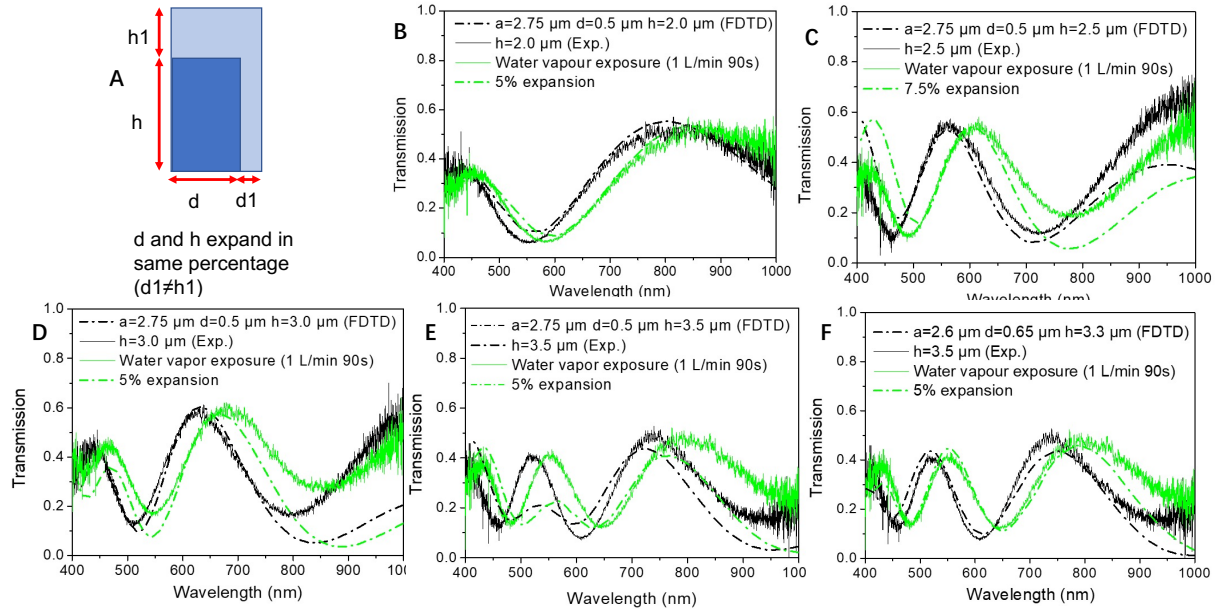

Figure S17. A) Schematic of expansion. **B) C) D)** and **E)** Transmission spectra of the photonic structures of design heights $h_{sim} = 2.0$ μm, 2.5 μm, 3.0 μm and 3.5 μm with film, before (black) and after 90 s in the presence of water vapour, where the gas vapour was transported using dry air at a flow rate of 1 L/min (green). The dash lines show the fitted FDTD simulations. F) The transmission spectrum of sample with $h_{design} = 3.5$ μm after adjusting the a, d and h values for the dry sample (black) while maintaining 5% expansion in d and h after 90s exposure to the water vapor (green).

In Figure 5, we present a simple optical pattern, achieved by just varying the height of the repeating array through a cycle of 1.5 μm, 2.0 μm, 2.5 μm, 3.0 μm, and 3.5 μm blocks. The SEM images of this array are presented in Figure S18 and provide a snapshot into the dynamic response of the array, caused by time dependent response of different blocks.
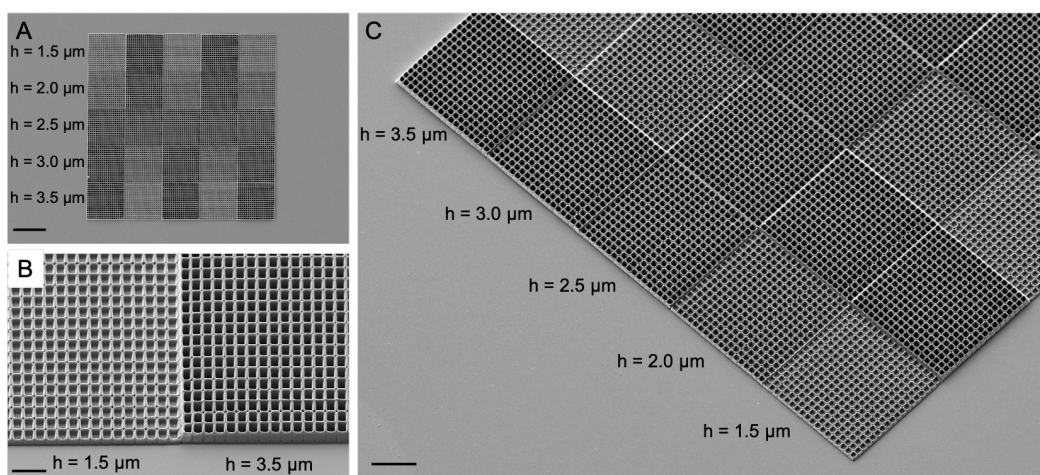
Figure S18. SEM images showing a 5 x 5 array containing 58 μm x 58 μm repetitive units of different design heights (h = 1.5 μm, 2.0 μm, 2.5 μm, 3.0 μm and 3.5 μm, respectively). Scale bar represents 50 μm in A, 10 μm in B and 20 μm in C. Images in B and C were achieved at a 40 degrees tilt and 30 degrees tilt, respectively.

References

1. Tudor, A.; Delaney, C.; Zhang, H.; Thompson, A. J.; Curto, V. F.; Yang, G.-Z.; Higgins, M. J.; Diamond, D.; Florea, L., Fabrication of soft, stimulus-responsive structures with sub-micron resolution via two-photon polymerization of poly(ionic liquid)s. Materials Today 2018, 21 (8), 807-816.

2. Habermann, C. E. Acrylamide. Kirk-Othmer Encyclopedia of Chemical Technology (2000).

3. Kim, Shin-Hyun, et al. Optofluidic assembly of colloidal photonic crystals with controlled sizes, shapes, and structures. Advanced materials 20.9 (2008): 1649-1655.

4.ChemicalBook, https://www.chemicalbook.com/ProductChemicalPropertiesCB4221908_EN.htm